Correlations between Ambient Noise and the Ocean Surface Wave Field

FRANCIS C. FELIZARDO

Department of Civil and Environmental Engineering, Massachusetts Institute of Technology, Cambridge, Massachusetts

W. KENDALL MELVILLE

Scripps Institution of Oceanography, University of California, San Diego, La Jolla, California

(Manuscript received 11 August 1993, in final form 31 March 1994)

ABSTRACT

Measurements of the ambient noise spectrum level N with simultaneous, coincident wind and wave measurements were made from RP *FLIP* in fall 1991. The measurements were designed to investigate the correlation between the ambient noise and relevant surface wave parameters. The results suggest that wave parameters related to the incidence of wave breaking correlated well with the ambient noise level. The correlation between N and the rms wave amplitude a was found to be poor but that between N and the rms amplitude of the local wind sea a_w was comparable to that between wind speed U and N. Similar good correlations were found between the rms wave slope s and N, and the higher frequency surface wave spectral levels and N.

Correlations between the surface wave dissipation estimates D based on the Hasselmann and Phillips models and the ambient noise were comparable to those between the wind speed and the ambient noise. The mean square acoustic pressure was found to be proportional to D^n with n in the range 0.5–0.8. The implications of these results for monitoring surface waves and air–sea fluxes are discussed.

1. Introduction

It is now believed that the sound generated by breaking waves is the primary source of the wind-dependent ambient noise in the ocean (Kerman 1988, 1992; Farmer and Vagle 1988, 1989). Yet, while decades of field measurements have shown a well-correlated power-law relationship between ambient noise and wind speed, very few measurements have tried to establish a similar correlation between ambient noise and surface wave field parameters. The few measurements that have attempted to do so show that the ambient noise does not correlate well with significant wave height. This is remarkable given that breaking waves are more directly related to the characteristics of the wave field rather than the wind. We believe that this is because swell and the longer wind wave components that do not break contribute a significant proportion to the variance of the wave field. In contrast, the laboratory measurements of Melville et al. (1988) and Loewen and Melville (1991) show that both sound generation and dissipation in breaking waves are correlated. Laboratory experiments of Lamarre and Melville (1991) imply that this correlation is due to the role of the entrained air in both the dynamics and acoustics of breaking waves. The aim of this work is to investigate whether comparable correlations hold in the ocean. To this end, we have conducted an experiment measuring ambient noise, wind, and the surface wave field from a floating platform off the coast of Oregon. These measurements are used to investigate the correlation between ambient noise and a number of surface wave parameters, especially surface wave dissipation, that are most directly related to breaking.

Pioneering underwater sound measurements by Knudsen et al. (1948) during World War II showed that the ambient noise spectrum level $N(f)$ in the 100–25 kHz range correlated with sea state. Their study resulted in what is now commonly referred to as the Knudsen curves, a family of curves showing approximately 20 dB per decade decrease in N within this range. A series of subsequent investigations [see Wenz (1962) and Urick (1986) for reviews] established a correlation between wind speed and N in the Knudsen range. Field measurements by Shaw et al. (1978) suggested that this relationship, described by an expression of the form

$$\log U = m(f)N(f) + n(f), \qquad (1.1)$$

can be used as a means of measuring the wind speed using hydrophones. In Eq. (1.1) U is the wind speed in meters per second, f is the frequency in Hertz, $m(f)$ and $n(f)$ are coefficients, and the noise spectrum level in dB re 1 μPa^2/1 Hz is

Corresponding author address: Prof. W. Kendall Melville, Scripps Institution of Oceanography, University of California at San Diego, La Jolla, CA 92093-0213.

TABLE 1. Coefficients for the WOTAN expression and the equivalent power laws obtained from previous field measurements.

f (kHz)	m	n	$10^{-3}m$	n
		Evans et al. (1984)		
4.3	0.0416	−1.497	4.0	2.4
8.0	0.0419	−1.329	1.5	2.4
14.5	0.0434	−1.217	0.64	2.3
		Lemon et al. (1984) site A		
4.3	0.0336	−1.045	1.29	3.0
8.0	0.0330	−0.925	0.64	3.0
14.5	0.0341	−0.810	0.38	2.9
		Lemon et al. (1984) site B		
4.3	0.0448	−1.64	4.6	2.2
14.5	0.0465	−1.23	0.44	2.2
		Vagle et al. (1990)		
8.0	0.0378	−1.006	0.46	2.7

$$N(f) = 10 \log\left[\frac{p^2(f)}{p_{\text{ref}}^2}\right], \tag{1.2}$$

where $p^2(f)$ is the ambient noise power spectrum, and $p_{\text{ref}}^2 = 1\ \mu\text{Pa}^2/1$ Hz. This technique, commonly referred to as *weather observations through ambient noise,* or WOTAN (Evans et al. 1984), has been used in several measurements over the last decade (e.g., Evans et al. 1984; Lemon et al. 1984; and Vagle et al. 1990).

While these studies confirmed the form of the expression in Eq. (1.1), they also showed some variability in the coefficients m and n. In addition, sound absorbed by bubbles generated by breaking waves were shown to cause significant departures from linearity at higher ambient noise frequencies and higher wind speeds (Farmer and Lemon 1984). The WOTAN expression coefficients from these experiments are summarized in Table 1. Although the WOTAN expression is dimensionally inhomogeneous, we can nonetheless rearrange Eq. (1.1) to relate U and N in terms of a power law of the form

$$\frac{p^2}{p_{\text{ref}}^2} = mU^n, \tag{1.3}$$

where $m = 10^{-n/10m}$ and $n = 1/10m$. Based on the values given in Table 1, we see that

$$p^2 \propto U^{2.2-3}. \tag{1.4}$$

Although the linear relationship between $N(f)$ and $\log U$ has been established by several decades of measurements, the physics behind this correlation cannot be gleaned from the WOTAN equation alone. While theoretical studies and laboratory experiments (Kerman 1988, 1992) have led to a growing consensus that the sound generated by breaking waves is responsible for the wind dependence of ambient noise in the Knudsen range, attempts at establishing a direct and predictable relationship between ambient noise and surface wave field parameters have been few and largely unsuccessful. Perrone's (1969) measurements gave a 0.8 correlation coefficient between U and N(0.2–2.8 kHz) while the correlation coefficient between the significant wave height H_s and N(0.2–2.8 kHz) was only 0.6. Farmer and Lemon (1984) obtained comparable correlation coefficients for H_s and ambient noise at 4.3, 8.0, and 14.5 kHz. By classifying measured wind velocities as steady, increasing, and decreasing, Penhallow and Dietz (1964) found that although U tracked the ambient noise at 630 Hz reasonably well under all these conditions, H_s correlated well only under steady conditions. Table 2 summarizes their results. Perhaps because of the relatively poor correlations between ambient noise and H_s obtained by the above studies, none of them published the coefficients of the regression between the two variables.

The poor correlation between N and H_s may appear surprising given that the ambient noise sources are direct products of the wave field itself. One should then expect that the correlation with wave parameters should be better than the wind speed correlation. This apparent discrepancy may partly be explained by the relatively large distance between the wave, wind, and N instruments in the above experiments. Perrone's (1969) wave and wind measurements were made 30 miles from the hydrophone site. Farmer and Lemon (1964) deployed their wave buoy approximately 10 km from their WOTAN. Penhallow and Dietz (1964), who made measurements close to shore, had the anemometers and wave gauges installed off a dock while the hydrophone was at 12-m depth, 300 m offshore. In this last case, shallow water effects may have also contributed to the acoustic measurements.

Perhaps the more plausible explanation is that the presence of swell increases H_s without proportionally increasing the incidence of wave breaking. Since swell is generated by storms far from the observation site, it is possible, particularly in the open ocean at long fetches, for H_s to be large even on a calm day with low wind speeds. Recent studies (e.g., Thorpe 1993; Melville 1994) suggest that it is the wind waves at fre-

TABLE 2. Linear correlation coefficients between N (630 Hz), H_s, and U (Penhallow and Dietz 1964).

	Steady winds		Decreasing winds		Increasing winds	
	U	H_s	U	H_s	U	H_s
N	0.90	0.90	0.80	0.66	0.79	0.42
U		0.88		0.67		0.47

quencies greater than the wind sea spectral peak that are breaking. If these models are correct, then wave components (including wind waves and swell) that do not break make a significant contribution to the variance of the sea surface displacement but not to the noise. If wave breaking is indeed primarily responsible for the ambient noise in the ocean, then correlations with N should be made with parameters that quantify wave breaking or are more directly related to that part of the wave spectrum directly affected by breaking.

Wave dissipation is perhaps the most important dynamical role of breaking waves. The relationship between the energy dissipated and the sound radiated by breaking waves was initially examined by Melville et al. (1988) for controlled breaking waves in the laboratory. This experiment, as well as the subsequent investigation by Loewen and Melville (1991) using a larger range of wave parameters, showed that the acoustic energy radiated by a breaking event is proportional to the surface wave energy dissipated by the event. In addition, Loewen and Melville (1991) showed that approximately 10^{-8} of the dissipated mechanical energy is converted to acoustic energy and that the energy of the radiated sound is proportional to the duration of the event.

Field measurements of the acoustic dipole source intensity (Kennedy 1992) suggest that the breaking wave acoustic spectrum is self-similar and is scaled by the friction velocity cubed (u_*^3), which is approximately proportional to the rate of energy dissipated by wave breaking (Phillips 1985). Kennedy's (1992) field measurements suggest that the ratio of acoustic energy to the dissipated wave energy is in the range 10^{-6}–10^{-8}.

By relating the electrical conductivity of an air–water mixture to the void fraction of the medium, Lamarre and Melville (1991) studied the evolution of bubble clouds formed by breaking waves. They found that up to 50% of the dissipated energy may be expended in entraining air against buoyancy forces. They also found that the energy dissipated by a breaking event was proportional to the initial volume of air entrained.

These studies clearly suggest that sound generation and the dissipation of mechanical wave energy are coupled by the air entrainment process. We believe that this is the reason why the two correlate well in the laboratory, and we expect that these two parameters should correlate in the field as well.

In the next section, we describe the field experiment conducted off the coast of Oregon to measure ambient noise, wind speed, and the wave field. Next, we examine correlations of the wave parameters with $N(f)$ and derive power laws for these relationships. We also examine the characteristics of the measured wave spectra and relate them to the wind. Later, we review the available dissipation models in the literature and obtain expressions for estimating dissipation using field data and examine how these estimates can be related to each other and to the ambient noise.

2. Experiment description

Simultaneous measurements of the surface wave spectrum, the ambient noise, the wind speed, and wind direction were made from the research platform *FLIP* approximately 130 km west of Reedsport, Oregon, in 3000 m of water on 26 September–7 October 1991 during the Noise on Basalts and Sediments Experiment (NOBS). *FLIP* was moored in a three-point configuration. The forces exerted by the surface waves, the underlying currents, and the mooring lines generated cyclical long period motions of *FLIP* that were picked up by our wire wave gauges and position sensors. These motions, primarily heave, pitch, and roll have previously been studied by Rudnick (1967). The effect of these motions on the wave gauge record is described in appendix A. At vertical attitude, 90 m of *FLIP* is submerged underwater. The section of hull that intersects the mean water line is approximately 3.8 m in diameter (Bronson and Glosten 1985). The surface waves reflected from the hull of the platform, which were observable by eye, did not appear to have a noticeable effect on the wave structure near the wave gauges 15 and 17 m away.

Figure 1 shows a schematic diagram of the location of the different instruments used. A hydrophone was mounted on *FLIP* 33 m below sea level. Because there was some concern that waves splashing on the hull might dominate the acoustic signal, it was considered desirable to use a directional hydrophone. This was accomplished by mounting an ITC-8181A omnidirectional hydrophone on the focus of a 42-inch double-walled parabolic dish. The centerline of the parabola was oriented upward at a 45° angle from the longitudinal axis of *FLIP*. The parabola was filled with foam to provide a reflecting surface and improve the directional characteristics of the hydrophone. The resulting beam pattern was obtained from a calibration at the Naval Ocean Systems Center Transducer Calibration Facility in San Diego, California (Felizardo 1993).

Prior to the start of each 10-minute sampling segment, the signal from the time code generator was sampled from the serial port of the PC and recorded. The hydrophone data was then sampled at 51.2 kHz using a TMS320C30 Real Time Board (Spectrum Signal Processing, Blaine, Washington). The power spectrum was computed by averaging nine 512-point FFTs every 0.1 sec, which were stored in two-byte integer records. The time code was sampled and recorded at the end of the segment prior to storing the data on 650MB magneto-optical disks.

The ambient noise spectrum level $N(f)$ for an equivalent omnidirectional hydrophone was computed from the raw power spectrum $R(f)$ using the formula

$$N(f) = R(f) - \mathrm{SA} - \mathrm{SL}(f) + \mathrm{AG}(f), \quad (2.1)$$

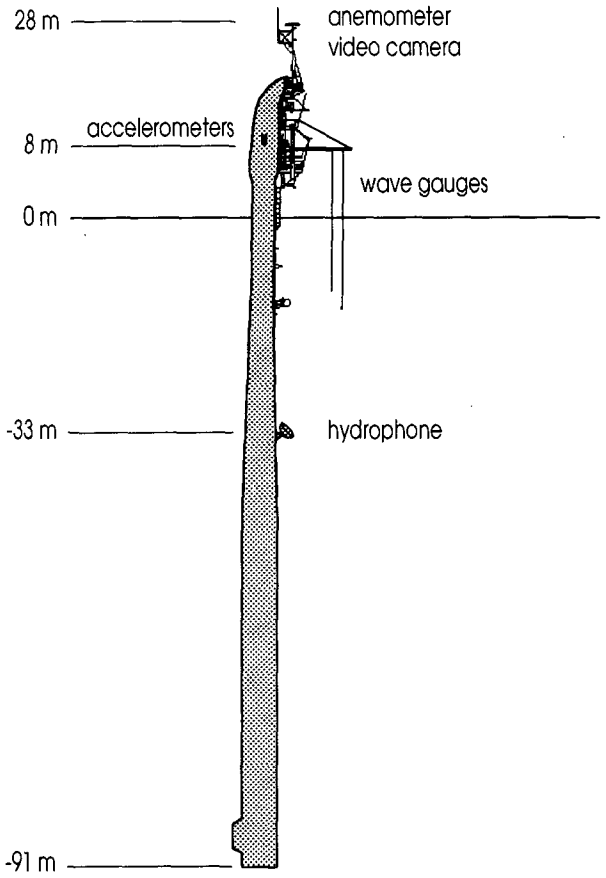

FIG. 1. A schematic diagram of *FLIP* showing the locations of the different instruments used in the experiment. The capacitance wire wave gauge is 15 m and the resistance wave gauge array is 17 m from the hull of *FLIP*.

where $R(f)$ is in dB re 1 volt^2/1 Hz, SA is the signal amplification (50 dB), SL is the hydrophone sensitivity level in dB re 1 μPa^2/1 volt^2, and the array gain,

$$\mathrm{AG} \equiv 10 \log \frac{\int_\Omega S d\Omega}{\int_\Omega S B^2(\Omega) d\Omega}, \qquad (2.2)$$

where Ω is the solid angle. In computing AG, radial symmetry was assumed in both hydrophone pattern B and sound source pattern S. Based on field measurements of the vertical directionality of ambient noise and a dipole sound source model, Urick (1986) suggested that the sound source pattern is proportional to $\cos\phi$, where ϕ is the angle from the vertical. Although we used Urick's (1986) model of S to compute AG, our computations also show that an omnidirectional sound source pattern will give AG values that differ from our results by less than 1 dB.

Figure 2 shows typical unsmoothed power spectra of the ambient noise in dB re 1 μPa^2/1 Hz. The spectra were averaged over one hour. The broad peak at 2.5 kHz is due to the high-pass filter. Much of the acoustic energy above 14 kHz is contaminated by electrical noise generated by other instruments on *FLIP*. The noise is difficult to eliminate so the $N(f)$ data presented will be primarily for frequencies less than 14.0 kHz.

The wind speed U and wind direction were measured using an anemometer mounted 28 m above sea level. This data, as well as the recorded wave gauge data were provided to us by Jerome Smith and Greg Bullard of SIO. One-hour averages of U were later computed and reduced to the wind speed at 10 m elevation U_{10}. In computing U_{10}, we assumed neutral atmospheric stability and used the wave age–dependent method described by Maat et al. (1991).

Two independent measurements of the surface waves were used. An array consisting of four Nichrome resistance wire wave gauges was deployed on a boom 8 m above the mean sea level and 17 m from the hull. The wires were suspended in a square configuration with 1-m diagonals. The ground wire was suspended at the center. A spreader was placed at the lower end of the wires to keep them apart. The wave slope calculations presented in this study use this data. A Tantalum capacitance wire wave gauge was also deployed along the boom 15 m from the hull and was calibrated in situ four times during the 12-day observation period. The field calibration of the capacitance wave gauge was accomplished by raising or lowering the wire at 0.5-m intervals, sampling the voltage for 50 s, and computing the mean voltage at each position. The resulting elevation versus voltage calibration curve was computed using a linear least squares fit of the sample points. An IMET Positional Sensor Package located in the working laboratory recorded the acceleration due to the motion of *FLIP*. This data was used to analyze

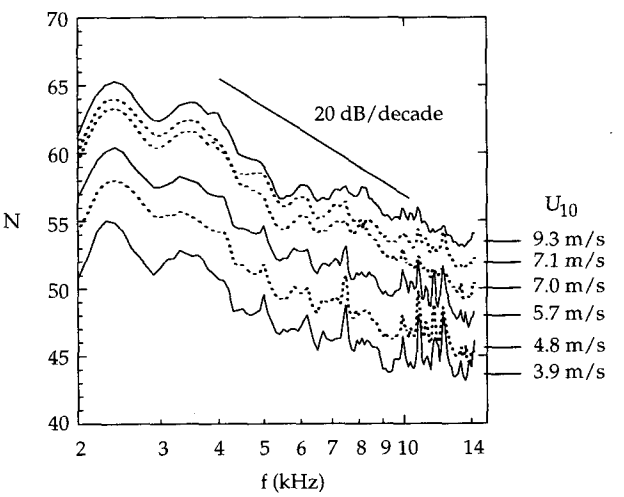

FIG. 2. Some typical unsmoothed ambient noise power spectra N [dB re 1 μPa^2/1 Hz] at various wind speeds. Each curve is computed from one hour of data.

the influence of the motion of *FLIP* on the wire wave gauge record. The signal from the wave gauges, the accelerometers, and the compass were low passed at 4 Hz and sampled at 8 Hz.

Figure 3 shows the characteristics of a typical wave height power spectrum observed during the experiment. The plot was obtained by computing and averaging 1024-point discrete Fourier transforms on a 1-h capacitance wire wave gauge record. Three major peaks are observed, with the higher frequency peaks due to swell and the wind sea. The peak below $f = \omega/2\pi = 0.05$ Hz is due to the 27-s heave and 48-s pitch–roll resonance of *FLIP*, which are unresolved. The presence of these peaks is consistent with previous studies of *FLIP*'s response to waves (Rudnick 1967). While the energy spectrum of *FLIP*'s motion due to waves has components of higher frequency, their effect on the measured wave energy at frequencies $f > 0.05$ Hz is small (see appendix A).

Figure 4 shows the characteristics of a typical wave slope power spectrum $\Gamma(\omega)$. The plot corresponds to a one-hour dataset sampled at 2000 UTC on Julian day 272 with $U_{10} = 9$ m s^{-1}. The wave slope was estimated from the finite difference of the sea surface elevations of the 4-wire wave gauge array. Details of the method are discussed in Felizardo (1993). The plot shows an agreement within a factor of 2 between $\Gamma(\omega)$ and the wave slope spectrum inferred from the wave height spectrum and linear dispersion $[k^2\Phi(\omega)]$ in the energy containing region of the slope spectrum $\omega = 0.2\pi$–1.6π rad s^{-1}.

3. Observations

The acoustic measurements were initiated on 26 September (Julian day 269) while winds blowing from the south were dying down. After one and a half days

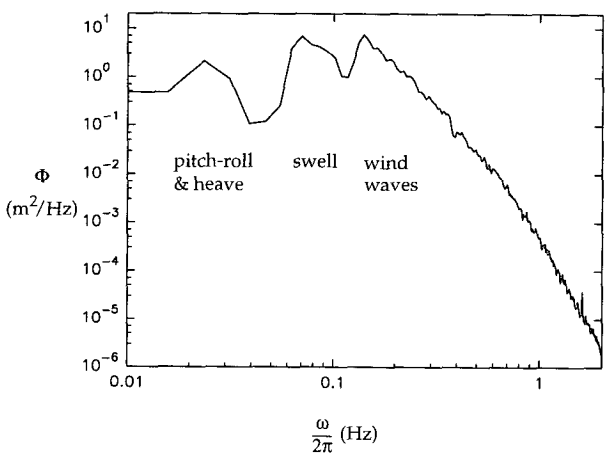

FIG. 3. Plot showing the characteristics of a typical 512-point wave height power spectrum. The data were sampled over one hour at 8 Hz with $U_{10} = 8$ m s^{-1}.

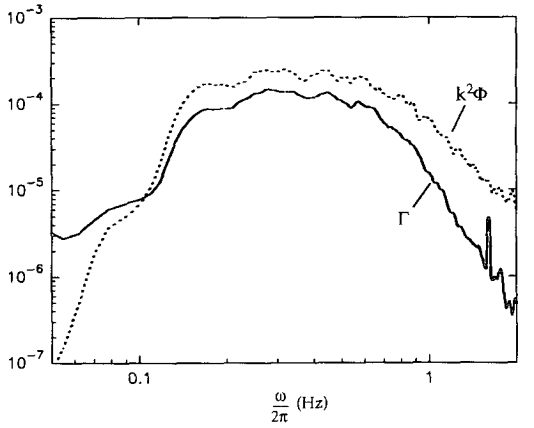

FIG. 4. Plot of a typical one-hour wave slope spectrum $\Gamma(\omega)$ [Hz^{-1}] with $U_{10} = 9$ m s^{-1} computed from the finite differences of the surface elevation measured by 4-wire array; $\Gamma(\omega)$ differs from $k^2\Phi(\omega)$ [Hz^{-1}] by a factor of 2 within the range $\omega = 0.2\pi$ to 2π.

of relative calm, the wind blew initially from the north (600-km fetch) with the wind speed increasing over a day. It remained quasi steady for a period of 6 days. The wind then changed direction and blew from the south (unlimited fetch) and then died down over the course of a day and a half. The effects of the sudden change in direction is clearly observable in the ambient noise record, the spectrum level of the wind wave frequencies, and to some extent, in the wave slope record. Figure 5 presents a time series of the wind speed U_{10}, the friction velocity u_*, and the wind direction.

a. Surface wave characteristics

As noted in section 2, the wave gauge record was contaminated by low-frequency energy due to the motion of *FLIP*. However, appendix A shows that this can be corrected by specifying a high-pass filter cutoff at $f = \omega/2\pi = 0.05$ Hz, and that the contribution of the platform motion to the wave gauge record above 0.05 Hz is small compared to the wave energy. In Fig. 6, we show the time series of some integral characteristics of the wave spectrum. The rms wave amplitude a and the mean radian frequency $\bar{\omega}$ of the surface wave spectrum were defined as

$$a = \left[\int_{\omega_0}^{\omega_N} \Phi(\omega)\, d\omega\right]^{1/2} \tag{3.1}$$

$$\bar{\omega} = \frac{\int_{\omega_0}^{\omega_N} \Phi(\omega)\,\omega\, d\omega}{\int_{\omega_0}^{\omega_N} \Phi(\omega)\, d\omega}, \tag{3.2}$$

where ω_N is the Nyquist radian frequency ($\omega_N = 2\pi f_N = 8\pi$ rad s^{-1}). In Figs. 6a and 6b, the lower integration limit was set to $\omega_0 = 0.1\pi$ rad s^{-1}. The values of a and $\bar{\omega}$ in both plots include energy from swell and wind

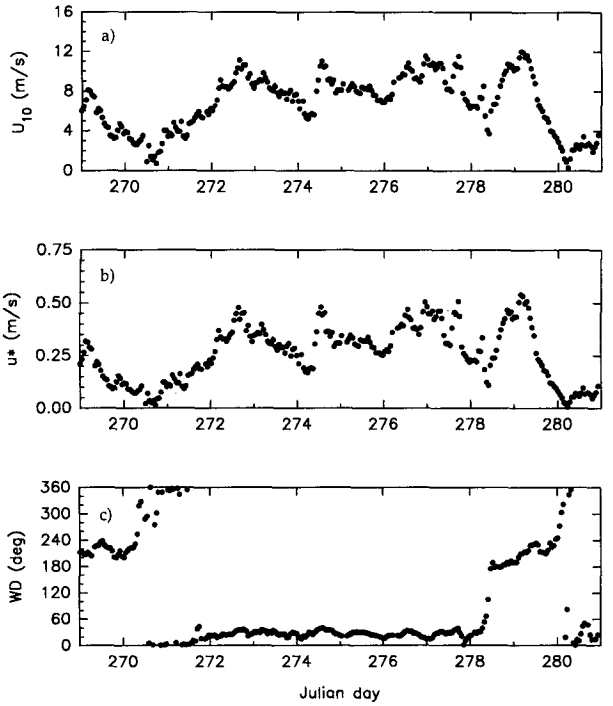

FIG. 5. Time series of U_{10}, u_*, and the wind direction during the NOBS experiment. Note that the wind rapidly changes direction on Julian day 278 after blowing from the north for approximately 6 days.

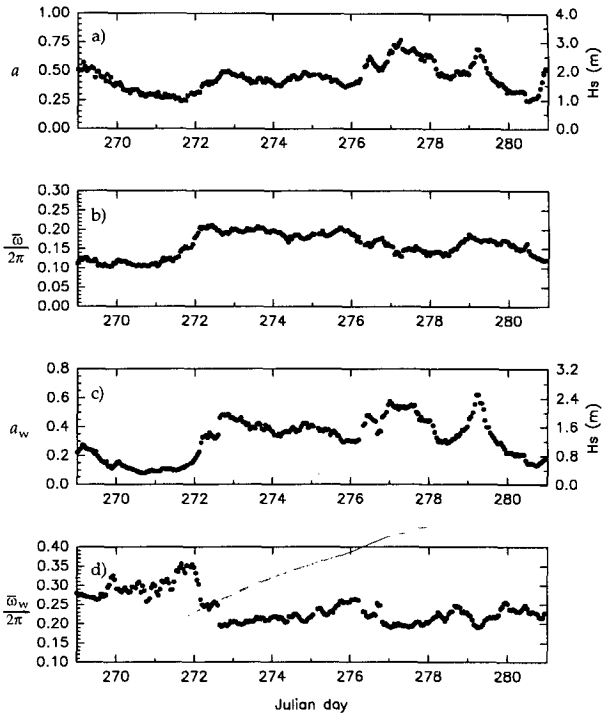

FIG. 6. (a) Rms amplitude a (m) and significant wave height H_s (m) computed from the full spectrum. (b) Mean frequency computed from the full spectrum $\bar{\omega}/2\pi$ (Hz). (c) Wave parameters a_w (m) and H_s (m) computed with swell filtered out. (d) Mean frequency with swell filtered out $\bar{\omega}_w/2\pi$ (Hz).

wave components. To eliminate the contribution of the swell to a and $\bar{\omega}$, ω_0 was set to the frequency between the wind wave and the swell peaks at which $\Phi(\omega)$ is a minimum.

The data in Figs. 6a and 6c are also presented in terms of the significant wave height H_s, defined as the highest one-third of waves (Longuet-Higgins 1952). For a Rayleigh-distributed wave field,

$$H_s = 4a, \tag{3.3}$$

to a very good approximation. Since the value of a includes swell components with characteristics unrelated to the local wind conditions, differences between the U_{10} and the a time series can clearly be observed, particularly during periods of low wind speed. For example, on Julian days 270 and 271, the value of a is large even though, as we see from Fig. 6c, the wind wave components have decayed. During this period, the value of a is dominated by swell.

We see from Figs. 5 and 6c that the time series of a_w looks qualitatively similar to that of U_{10}. The similarities in the time series of U_{10} and a_w suggest that by eliminating swell, we obtain a measure of the wave field that more closely reflects the interaction between the wind and the wave field.

Figure 7 shows the time series of the spectral level of Φ at π, 1.5π, and 2π rad s^{-1}. These plots show the variability of the wave energy above the wind wave peak. The similarities between the time series of these parameters and U_{10} is also apparent here.

Figure 8 shows the time series of rms wave slope s. This was obtained from the variance of the finite differences of the surface elevations between the different resistance wire wave gauges.

Figure 9 shows 12 spectra taken from one-hour samples of the wave gauge record at the start of each day during the observation period. Following Phillips (1985), $\Phi(\omega)$ and ω were put in dimensionless form with

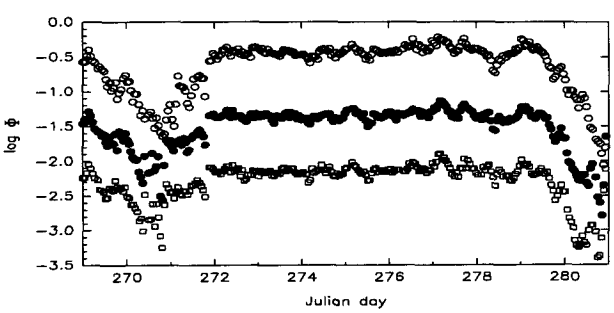

FIG. 7. Time series of the log of the surface wave spectrum level logΦ [m^2/Hz] at selected frequencies: π rad s^{-1} (○), 1.5π rad s^{-1} (●), 2π rad s^{-1} (□).

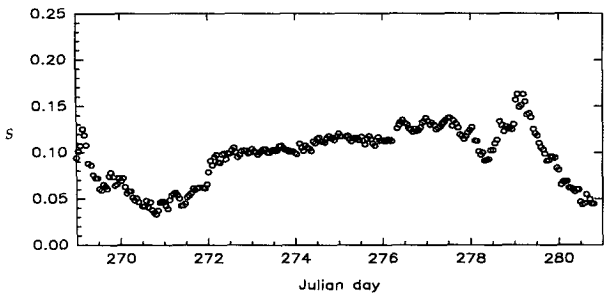

FIG. 8. Time series of the rms wave slope s computed from the resistance wire wave gauge array data.

$$\tilde{\Phi} \equiv \frac{\Phi g^3}{u_*^5} \quad \text{and} \quad \tilde{\omega} \equiv \frac{u_* \omega}{g}. \tag{3.4}$$

Phillips (1985) suggested that for the surface wave frequencies above the spectral peak, the interaction of wind forcing, dissipation, and spectral flux can be described by an equilibrium balance that gives a surface wave frequency spectrum

$$\Phi_E = \alpha u_* g \omega^{-4},$$

where α is the Toba coefficient. From a survey of several field investigations, Phillips (1985) concluded that α is in the range 0.06–0.11. Using this nondimensionalization, the equilibrium wave spectrum becomes

$$\frac{\Phi_E g^3}{u_*^5} = \alpha \left(\frac{u_* \omega}{g} \right)^{-4}. \tag{3.5}$$

In Fig. 9, the upper and lower limits of Eq. (3.5) are plotted as solid lines. The figure suggests that for our data, α is closer to the upper limit of the range suggested by Phillips (1985). The plots show a close agreement between the equilibrium spectrum and the measured spectra in the frequency range between ω_p, the frequency at the peak of the spectrum, and approximately $2.5\omega_p$, where the measured spectral slope is approximately ω^{-4}. For $\omega > 2.5\omega_p$, the slope of the wave spectrum appears to be closer to $\Phi(\omega) \sim \omega^{-7}$.

Phillips (1985) also predicted that the upper limit of the ω^{-4} slope is determined by the presence of wind drift $q \approx u_*$, which would inhibit the creation of waves whose phase speed is comparable to u_* [see section 4b(1)]. He proposed that the wavenumber of this upper limit is

$$k_1 = \omega_1^2 / g = r g / u_*^2, \tag{3.6}$$

where r is a constant. He suggested that $r > 0.16$ for typical wind waves. Rearranging Eq. (3.6) gives

$$\frac{\omega_1 u_*}{g} = r^{0.5} \approx 0.4, \tag{3.7}$$

which is 2–3 times the value of the upper limit of the equilibrium range in Fig. 9. While the data show that there is an upper limit to the ω^{-4} spectral slope, other mechanisms apart from wind drift may be responsible.

b. Ambient noise

Figure 10 presents the time series for the acoustic data at selected frequencies. We have chosen to display N at 4.3, 8.0, and 14.0 kHz since these are the common WOTAN frequencies (see Table 1). The total integrated acoustic energy between 2.5–14 kHz denoted by Σ is also presented. Note that the wind speed fluctuation due to the rapid change in wind direction (day 278) is clearly observed in the acoustic record. A comparison between Fig. 10 and Fig. 5 shows that, consistent with the previous WOTAN experiments reviewed in section 1, changes in the time series of U_{10} and u_* are clearly reflected in the time series for N. Similarities between the acoustic record and some of the wave parameters, particularly a_w, s, $\Phi(\pi)$, $\Phi(1.5\pi)$, and $\Phi(2\pi)$ can also be seen. This will be clearer in section 3c when we examine the empirical relationships between N and the wave parameters.

c. Comparisons with ambient noise

Figure 11 shows plots of $\log U_{10}$ versus the spectrum level at the different ambient noise frequencies $N(f)$ given in Fig. 10 showing a linear relationship between the two parameters. We also plotted the regression lines from the different WOTAN measurements given in Table 1 and from our data. The regression equations were computed from the data using an orthogonal least squares fit (Casella 1990, p. 584) since both $\log U_{10}$ and $N(f)$ are random variables. A summary of the linear regression coefficients and the power-law coefficients are given in Table 3. The equation of the regression lines for our data are comparable to those found by

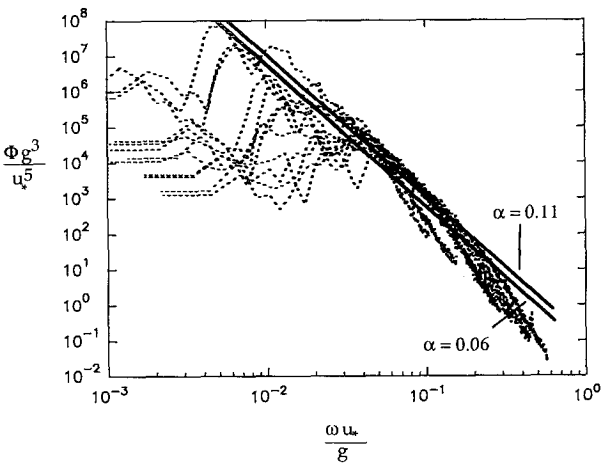

FIG. 9. A selection of typical nondimensional 1-h wave spectra. The spectra were taken from wave height records sampled at the start of each day. The solid lines denote Φ_E with $\alpha = 0.06$ and 0.11.

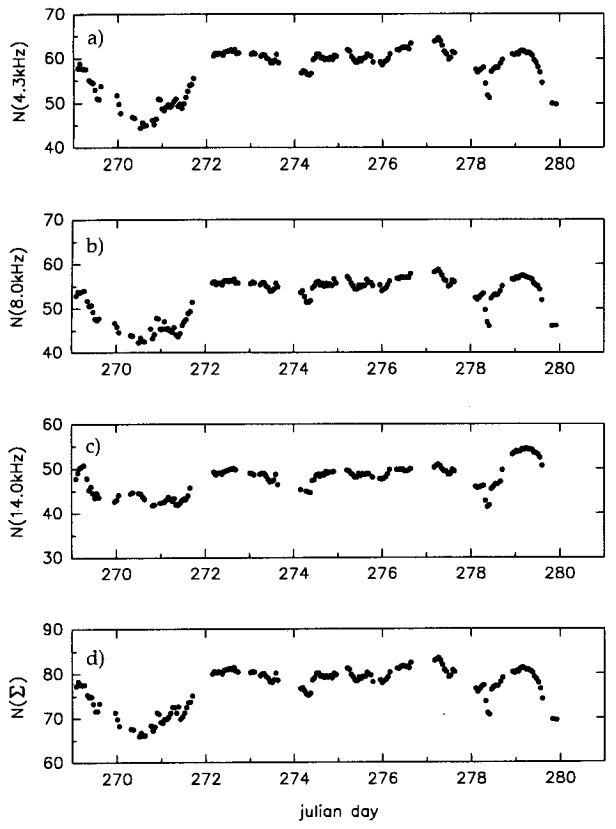

FIG. 10. Time series of the ambient noise spectrum level N [dB re 1 μPa^2/1 Hz] at selected WOTAN frequencies. Note the similarities between these time series and the U_{10} time series. In particular, note the rapid drop and increase in N on Julian day 278: (a) 4.3 kHz, (b) 8.0 kHz, (c) 14.0 kHz, (d) wide band (2.5–14 kHz or Σ).

previous investigators. Our results suggest an ambient sound pressure level dependence of

$$p^2 \propto U_{10}^{2.4-3.0}. \tag{3.8}$$

The data give correlation coefficients $C_{xy} \approx 0.94$ between $\log U_{10}$ and $N(f)$ except at 14 kHz where $C_{xy} = 0.78$. The lower value of C_{xy} and the larger scatter in the data at 14 kHz is probably due to the higher level of noise at that frequency. This is evident in Fig. 2, especially for the spectra at lower wind speeds. Except for the 14 kHz data, which appears to exhibit more scatter than the data at the other ambient noise frequencies, the relationship between the different N frequencies and U_{10} are qualitatively similar. The same is also observed in the comparisons between N and other wind and wave parameters. Hence, subsequent plots will show only the N (4.3 kHz) data.

The relationship between ambient noise N and the friction velocity u_* can similarly be obtained. This is shown in Fig. 12 and Table 4, which suggest that a linear fit to the data is adequate. They also suggest that the mean square acoustic pressure can be related to u_* by

$$p^2 \propto u_*^{1.8-2.3}. \tag{3.9}$$

The novel aspects of this work, however, are in the empirical relationships between ambient noise and wave parameters. As mentioned above, previous field experiments (Penhallow and Dietz 1964; Perrone 1969; Farmer and Lemon 1984) found that ambient noise and significant wave height (or alternatively, the rms wave amplitude a) were poorly correlated. The plot in Figure 13a, which compares our measurements of N and a, are consistent with their results. We suggested earlier that the presence of acoustically inactive swell reduces the correlation between N and a. While swell significantly increases a, it does not proportionally increase the characteristic steepness of the waves, although mechanisms of long wave–short wave interaction may increase the incidence of wave breaking.

To reduce the influence of swell on the variance of the wave field, we filtered it out and computed only the rms amplitude of the wind wave components a_w. The resulting a_w estimate, whose time series is shown in Fig. 6c, is plotted against N in Fig. 13b. We see from this figure that although the scatter in the data is greater than that between U_{10} and N, the improvement in the correlation between the surface wave amplitude and N is significant. Table 5 shows that the power-law relationship is given by

$$p^2 \propto a_w^{1.8-2.2}. \tag{3.10}$$

We can better understand the relationship between wind speed and wind waves by examining the behavior of the high frequency wave components. Figure 7 shows that the time series of the surface wave spectrum level in the wind wave frequencies closely match the characteristics of both the U_{10} and the N time series. Figure 14 shows plots of the ambient noise at 4.3 kHz and $\Phi(\pi)$, $\Phi(1.5\pi)$, $\Phi(2\pi)$. The data give correlation coefficients C_{xy} equal to 0.92, 0.90, and 0.87, respectively. Plots of the wind wave spectral level and N at 8 kHz and Σ (2.5–14 kHz band) are qualitatively similar.

Our results show that a and N are poorly correlated partly because of the presence of swell. The characteristics of swell are not directly determined by the local wind and wave relationship and its influence on the noise generation mechanisms is weak. By neglecting swell and concentrating on the wind wave region of the spectrum, we can obtain a better-correlated power-law relationship between N and a_w. This is clearly shown by the improved correlation between the higher frequency surface wave spectral level and N.

Experiments by Rapp and Melville (1990) and Loewen and Melville (1991) have shown that the prebreaking wave slope can be used to measure the strength of wave breaking in a laboratory wave tank. Their experiments suggest that the wave slope correlates with several dynamical characteristics of breaking, for example, loss of excess momentum, mixing, dissipation, and noise generation. These results suggest that

the overall steepness of the wave field is an important indicator of the characteristics of wave breaking.

The time series of the rms wave slope s in Fig. 8 shows qualitative similarities with both the U_{10} and the ambient noise time series. In Fig. 15, log$s$ is plotted against N(4.3 kHz). The plot shows that the ambient noise increases with the rms wave slope s. The characteristics of this relationship are summarized in Table 6, which shows that if we neglect the N(14 kHz) record, C_{xy} is greater than 0.85 and the two parameters can be related by the power law

$$p^2 \propto s^{3.1-3.4}. \tag{3.11}$$

4. Dissipation estimates

Although direct measurements of the total dissipation due to wave breaking in the field are not yet feasible, dissipation can be estimated using energy budgets arising from wind–wave evolution models. If terms other than dissipation can be effectively measured or modeled, then the dissipation can be inferred through an approximate energy or action balance.

TABLE 3. Some coefficients for the WOTAN expression and the equivalent power laws computed from NOBS data (cf. Table 1 and Fig. 11) for $\log U_{10} = mN + n$ and $p^2/p^2_{\text{ref}} = mU_{10}^n$.

f (kHz)	C_{xy}	m	n	$10^{-3}m$	n
4.3	0.94	0.0336	−1.089	1.7	3.0
8.0	0.93	0.0367	−1.157	1.4	2.7
14.0	0.78	0.0417	−1.261	1.1	2.4
Σ	0.94	0.0376	−2.057	296	2.7

The evolution of the surface wave field can be represented by (Phillips 1985)

$$\rho_w g \frac{d\Psi(\mathbf{k})}{dt} = \rho_w g \frac{\partial \Psi}{\partial t} + \rho_w g(\mathbf{c}_g + \mathbf{V}) \cdot \nabla_{\mathbf{k}} \Psi = -\nabla_{\mathbf{k}} \cdot T(\mathbf{k}) + w(\mathbf{k}) - d(\mathbf{k}), \tag{4.1}$$

where ρ_w is the density of water, g is the gravitational acceleration, $\mathbf{c}_g$ is the group velocity of the surface waves, and $\mathbf{V}$ is the current velocity. The three forcing

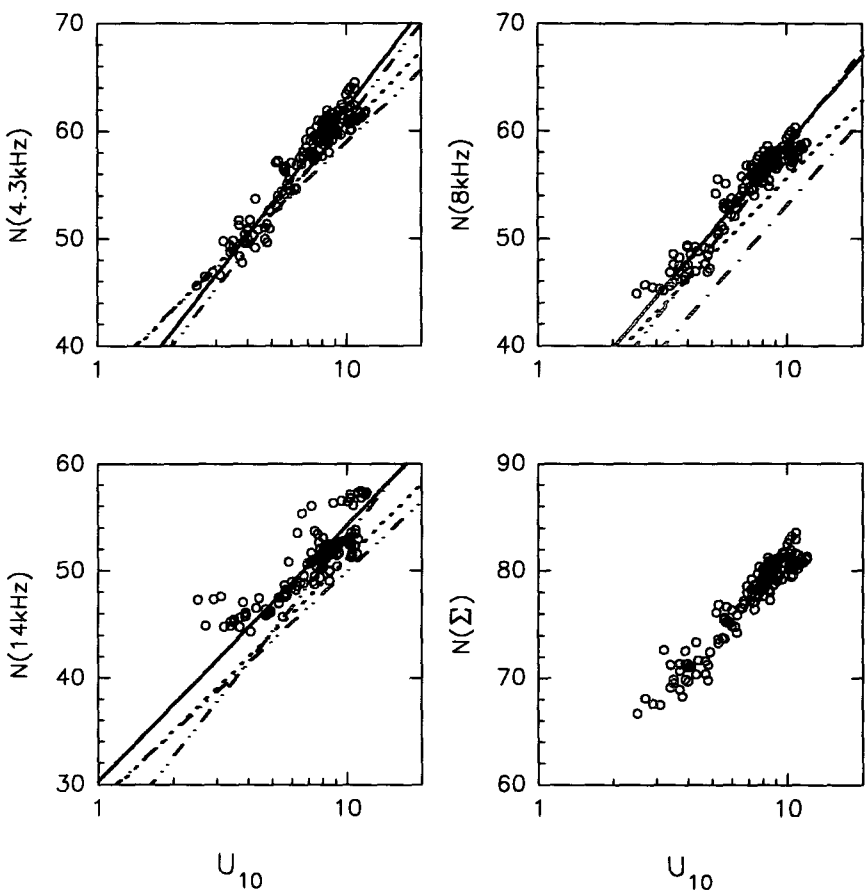

FIG. 11. Plot of U_{10} (m s^{-1}) vs selected N (dB re 1 μPa^2/1 Hz) frequencies. Lines indicate regression equations obtained in previous investigations (see Table 1). This study: solid line, Evans et al (1984): short dash, Lemon et al (1984): dash-dot-dot, Vagle et al (1990): dash-dot.

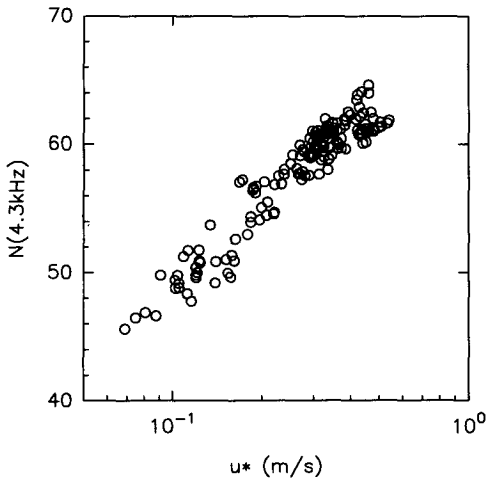

FIG. 12. Plot of u_* (m s^{-1}) vs N(4.3kHz) [dB re 1 μPa^2/1 Hz] showing a good correlation between u_* and N.

terms on the right-hand side are the net spectral flux from resonant wave–wave interactions, the spectral wind-forcing term w, and the spectral dissipation term d. The expression for the wave–wave interactions was first developed by Hasselmann (1962, 1963) and it involves computing the collision integral relating the component wavenumbers. Semi-empirical expressions for w based on field measurements of pressure fluctuations and the Miles (1957) wind wave generation model were proposed by Snyder et al. (1981) and by Plant (1982). It is generally believed that the expression for d is the least understood component of Eq. (4.1).

a. *Spectral dissipation models*

1) PHILLIPS (1985)

Phillips (1985) assumed that for the higher frequency components of the wave field (wind waves), the temporal and spatial scales for growth and decay are significantly longer than the internal wind wave time and length scales. He then argued that these waves are essentially in equilibrium, and the three source terms are proportional and are of comparable order

$$-\nabla_{\mathbf{k}} \cdot T(\mathbf{k}) \propto w(\mathbf{k}) \propto d(\mathbf{k}). \tag{4.2}$$

TABLE 4. Linear regression coefficients relating log u_* and N, and the equivalent power laws computed from NOBS data (cf. Fig. 12) for $\log u_* = mN + n$ and $p^2/p_{\text{ref}}^2 = mu_*^n$.

f (kHz)	C_{xy}	m	n	$10^{-3}m$	n
4.3	0.95	0.0443	−3.138	12.1	2.3
8.0	0.95	0.0485	−3.228	4.5	2.1
14.0	0.86	0.0554	−3.384	1.3	1.8
Σ	0.95	0.0496	−4.420	815	2.0

Using a simplified spectral flux expression and the Plant (1982) wind input formula, he showed that the equilibrium forms for the wavenumber and frequency spectra are

$$\Psi_E(\mathbf{k}) = \beta(\cos\theta)^p u_* g^{-1/2} k^{-7/2} \tag{4.3}$$

$$\Phi_E(\omega) = \alpha u_* g \omega^{-4}, \tag{4.4}$$

where α is the Toba coefficient. Based on a survey of various field measurements, Phillips (1985) concluded that the value of α is in the range 0.06–0.11. Figure 9 shows that for our measurements, $\alpha \approx 0.11$. The value of β is obtained from the equation $\beta = \alpha/4I(p)$, which relates the magnitudes of the frequency and wavenumber spectra, and the surface wave spreading function

$$I(p) = \int_{-\pi/2}^{\pi/2} (\cos\theta)^p d\theta. \tag{4.5}$$

Using the same assumptions, Phillips (1985) then showed that the spectral dissipation term in Eq. (4.1) is

$$d_p(\mathbf{k}) = \rho_w \gamma g k^8 \Psi^3(\mathbf{k}), \tag{4.6}$$

where γ is obtained from the assumption that $w(\mathbf{k})$ is comparable to $d(\mathbf{k})$, with $\gamma\beta^2 \approx 0.04$. Since our wave data are in terms of the frequency spectrum $\Phi(\omega)$, we need to express $d(\mathbf{k})$ in terms of Φ and ω. Substitution of Eq. (4.3) into Eq. (4.6) and use of the deep water linear dispersion relation $\omega^2 = gk$ gives

$$d_p(\omega) = \frac{I(3p)\rho_w g^{-3}\gamma}{16[I(p)]^3}\, \omega^{11}\Phi^3(\omega). \tag{4.7}$$

The details of the transformation can be found in Felizardo (1993). The total dissipation can therefore be computed from the measured wave spectrum,

$$D_p = \int_\omega d_p(\omega)d\omega = \frac{I(3p)\rho_w g^{-3}\gamma}{16[I(p)]^3} \int_{\omega_p}^{\infty} \omega^{11}\Phi^3(\omega)d\omega. \tag{4.8}$$

The lower limit of the equilibrium range was assumed to be the spectral wind wave peak. The integral in Eq. (4.8) will converge as long as the spectral slope of $\Phi(\omega)$ is steeper than ω^{-4} as $\omega \to \infty$.

By using the equilibrium expression for the surface wave frequency spectrum Φ_E [Eq. (4.4)], we can obtain an expression for the total dissipation based on integral wind and wave parameters E_p. Substitution of Eq. (4.4) into Eq. (4.8) gives

$$E_p = 4\gamma\beta^3 I(3p)\rho_w u_*^3 \int_{\omega_p}^{\omega_1} \omega^{-1} d\omega. \tag{4.9}$$

The value of the integral will be infinite unless a finite upper limit ω_1 is introduced. Phillips (1985) argued that this upper limit is determined by the presence of

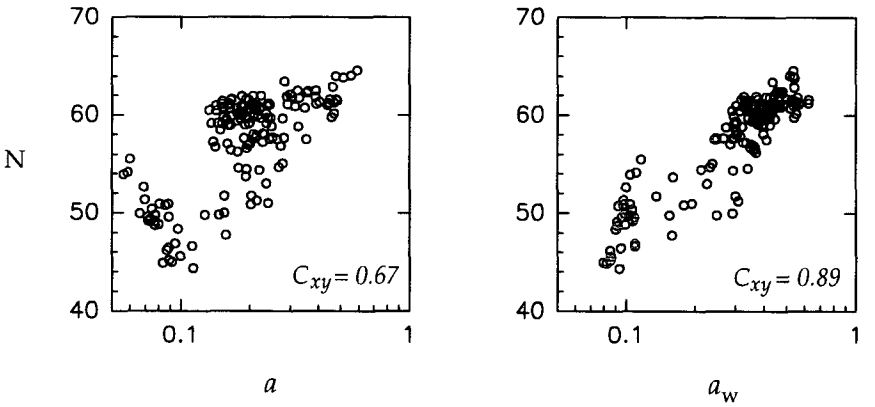

FIG. 13. The correlation between the surface wave amplitude and N is improved by neglecting the contribution of swell. The correlation coefficients C_{xy} are shown for each plot. (a) Plot of N(4.3 kHz) (dB re 1 μPa^2/1 Hz) vs the rms amplitude a [m]. (b) Plot of N(4.3kHz) vs the rms wind wave amplitude a_w [m].

wind drift q, which suppresses the formation of high frequency waves traveling at the same velocity. He suggested that, based on the work of Keulegan (1951), $q \approx u_*$ and the upper limit $\omega_1 = r^{1/2} g/u_*$, where r is a constant of order one. Integration of Eq. (4.9) and using the lower limit $\omega_p = g/c_p$ gives

$$E_p = 2\gamma\beta^3 I(3p)\rho_w u_*^3 \ln\left[r\left(\frac{c_p}{u_*}\right)^2\right]. \quad (4.10)$$

The difficulty in modeling the characteristics of the directional distribution of the wave field contributes to some uncertainty in the Phillips dissipation estimate. Based on field measurements, Phillips (1985) suggested that the lower and upper bounds of the directional spreading parameter p in Eq. (4.8) are 0.5 and 2, respectively. If $p = 0.5$, then $\gamma = 302$ and $I(3p)\gamma/[I(p)]^3 = 38$. If $p = 2$, then $\gamma = 131$ and $I(3p)\gamma/[I(p)]^3 = 33$. The upper and lower bounds of Eq. (4.8) differ by less than 20%. In Eq. (4.10), the value of E_p is controlled largely by the coefficient $\gamma\beta^3 I(3p)$ whose value is determined by p and by α. It is easy to show that the lower limit of this coefficient is obtained when $(p, \alpha) = (2, 0.06)$ and the upper limit when $(p, \alpha) = (0.5, 0.11)$. Consequently, $\gamma\beta^3 I(3p)$ is expected to be in the range 3.7–8.0 $\times$ 10^{-4}, giving an uncertainty of a factor of $\sim$2.

TABLE 5. Linear regression coefficients relating log a_w and N, and the equivalent power laws computed from NOBS data (cf. Fig. 13b) for $\log a_w = mN + n$ and $p^2/p_{\text{ref}}^2 = ma_w^n$.

f (kHz)	C_{xy}	m	n	$10^{-3}m$	n
4.3	0.89	0.0450	−3.126	8.8	2.2
8.0	0.89	0.0496	−3.236	3.3	2.0
14.0	0.77	0.0547	−3.297	1.1	1.8
Σ	0.87	0.0494	−4.348	633	2.0

2) HASSELMANN (1974)

Hasselmann (1974) argued that, although wave breaking is locally a highly nonlinear process, it is in general "weak in the mean" and that to lowest order, the spectral dissipation should be a quasi-linear function of Φ and a damping coefficient proportional to the square of the frequency ω; that is,

$$d_H(\omega) = -\eta\omega^2\Phi(\omega), \quad (4.11)$$

where η is a constant. Komen et al. (1984, herein referred to as KHH) proposed an expression for the coefficient η that they obtained by performing numerical simulations on the forms of η to simulate fetch-limited wave growth and reproduce the characteristics of a Pierson–Moskowitz spectrum between ω_p and $2.5\omega_p$. WAMDIG (1988) describes a numerical implementation of a wave evolution model using a numerically

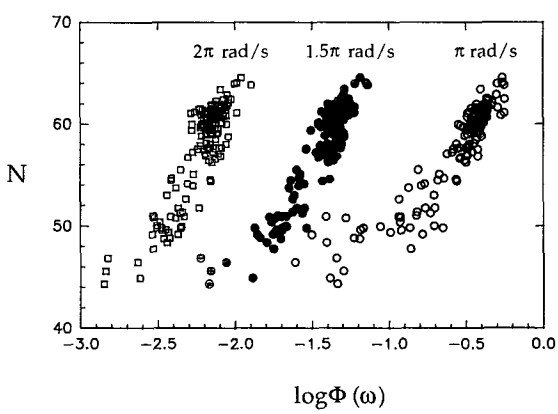

FIG. 14. The log of the spectrum level of the wind wave frequencies $\log\Phi(\omega)$ (m^2 Hz^{-1}) and N are well correlated. The plots show comparisons between N(4.3 kHz) and $\Phi(\pi$ rad s$^{-1})$: O, $\Phi(1.5\pi$ rad s$^{-1})$: ●, and $\Phi(2\pi$ rad s$^{-1})$: □.

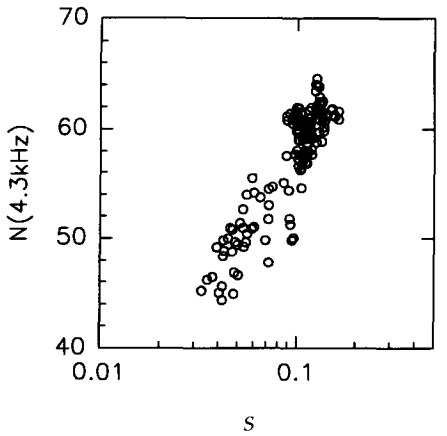

FIG. 15. Plot of the rms wave slope s vs the ambient noise N.

stable form of the KHH dissipation expression. While the WAMDIG expression is slightly different from the KHH formula, it is based on the same assumptions and gives dissipation estimates that are of the same order of magnitude as the KHH formula. KHH suggested that the total dissipation due to wave breaking is

$$D_H = \rho_w g \int_{\omega_0}^{\infty} c_H(\omega/\bar{\omega})^2(\bar{\alpha}/\bar{\alpha}_{PM})^2\bar{\omega}\Phi(\omega)d\omega, \quad (4.12)$$

where $\bar{\alpha} = e\bar{\omega}^4/g^2$ is a measure of the wave steepness, $\bar{\alpha}_{PM} = 4.57 \times 10^{-3}$ is the value of $\bar{\alpha}$ for a fully developed wind sea based on the Pierson–Moskowitz spectrum, $\rho_w = 1025$ kg m^{-3} is the density of seawater, $e = \int_\omega \Phi(\omega)d\omega$ is the total surface wave energy, and

$$\bar{\omega} = \frac{\int_\omega \Phi\omega d\omega}{\int_\omega \Phi d\omega} \quad (4.13)$$

is the mean frequency of the wave spectrum. Based on Figs. 4 and 5 of KHH, we estimate that c_H is in the range 3–6($\times 10^{-5}$) with $c_H = 3.33 \times 10^{-5}$ being the optimum value for Φ to approximate the Pierson–Moskowitz spectrum.

3) Reduced Hasselmann dissipation

In many instances, the full wave spectrum is not available. Instead, the summary wave data is limited to a few variables, for example, rms wave amplitude a (or significant wave height) and the mean radian frequency of the wave spectrum $\bar{\omega}$. We can use these parameters to obtain a dissipation estimate by assuming that the frequency spectra in either Eq. (4.12) can be approximated by a simple ω power law.

We assume an idealized wave spectrum of the form

$$\Phi_M(\omega) = mu_* g\omega^{-4}, \quad \omega > \omega_p, \quad (4.14)$$

TABLE 6. Linear regression coefficients relating log s and N, and the equivalent power laws computed from NOBS data (cf. Fig. 15) for $p^2/p_{\text{ref}}^2 = ms^n$.

f (kHz)	C_{xy}	$10^{-8}m$	n
4.3	0.87	18.5	3.4
8.0	0.88	2.9	3.1
14.0	0.81	0.23	2.6
Σ	0.85	802	3.1

where m is a constant. Note that Eq. (4.14) implies that only the contribution by the wind wave components are being considered in the reduced KHH estimate. Enforcing Parseval's theorem,

$$a^2 = \int_0^{\infty} \Phi(\omega)d\omega \quad (4.15)$$

gives

$$\Phi_M(\omega) = 3a_w^2\omega_p^3\omega^{-4}, \quad \omega \geq \omega_p. \quad (4.16)$$

The relationship between $\bar{\omega}$ and ω_p is obtained by substituting Eq. (4.14) into the definition of $\bar{\omega}$ [Eq. (4.13)]. For a spectrum with an ω^{-4} tail,

$$\bar{\omega} = 1.5\omega_p. \quad (4.17)$$

Substitution of Eqs. (4.16) and (4.17) into Eq. (4.12) gives the equation for the reduced KHH dissipation

$$E_H = 1.333\rho_w g c_H\left(\frac{\bar{\alpha}}{\bar{\alpha}_{\text{PM}}}\right)^2 a_w^2\bar{\omega}_w. \quad (4.18)$$

Table 7 summarizes the four total dissipation estimates discussed in this section; D denotes the total dissipation computed from the measured wave height spectrum, whereas E denotes the total dissipation computed from wind and integral wave parameters (the reduced estimate).

b. Total dissipation estimates

Figure 16 shows the time series of the four dissipation estimates described above using measurements from our experiment. In computing the Phillips dissipation estimate, we used $p = 0.5$ and $\alpha = 0.11$, which from section 4a(1) implies that $I(p) = 2.4$, $I(3p) = 1.75$, $\beta = 0.0115$, $\gamma = 302$, and $r = 0.16$. Based on the dis-

TABLE 7. Formulas used in estimating dissipation.

$$D_P = \frac{I(3p)\rho_w g^{-3}\gamma}{16[I(p)]^3}\int_{\omega_p}^{\infty}\omega^{11}\Phi^3(\omega)d\omega$$

$$E_P = 2g\beta^3 I(3p)\rho_w u_*^3 \ln[r(c_p/u_*)^2]$$

$$D_H = \frac{\rho_w g c_H(\bar{\alpha}/\bar{\alpha}_{PM})^2}{\bar{\omega}_w}\int_{\omega_0}^{\infty}\omega^2\Phi(\omega)d\omega$$

$$E_H = 1.33\rho_w g c_H(\bar{\alpha}/\bar{\alpha}_{PM})^2 a_w^2\bar{\omega}_w$$

cussion in section 4a(1), these values are near the upper limit of D_P and E_P. The figure shows that although the four equations (D_P, E_P, D_H, E_H) are based on different assumptions regarding the spectral characteristics of dissipation, these equations give comparable estimates of the total dissipation over most of the measured wind and wave conditions during NOBS.

Figure 16a shows very good agreement between the full and reduced KHH estimates (D_H and E_H). The two time series are virtually indistinguishable through most of the observation period. Although there is reasonably good agreement between D_P and E_P (Fig. 16b), there can be significant differences between the two, particularly during periods of rapid wind and wave growth and decay. Figure 16c shows that D_P is larger than D_H by a nearly constant factor of ~ 2. However, these dissipation estimates are within the same order of magnitude and the differences are small compared to the dynamic range of the data. Moreover, given the factor of 2 uncertainty in D_H [see section 4a(2)] and the 20% uncertainty in D_P based on the Phillips (1985) estimates of the empirical constants [see section 4a(1)], the agreement between D_P and D_H is good.

These time series comparisons (Fig. 16a–d) show that the different estimates agree well under steady wind and wave conditions but may vary significantly during periods of rapid wave growth or decay. The closeness of these values is not surprising since Phillips (1985) and the KHH chose the coefficients of the expressions so that the dissipation, the wind input, and the nonlinear flux expressions are of comparable order.

1) D_H AND E_H

In section 4a(3), we showed how E_H was derived by substituting an idealized ω^{-4} spectrum in the KHH dissipation expression [Eq. (4.12)]. The mean frequency $\bar{\omega}$ and the variance a^2 of the idealized spectrum are equal to those of the wind wave portion of the measured spectrum. Most of the differences between D_H and E_H arise because in deriving E_H, we chose not to model the dissipation below the wind wave spectral peak. The total energy in the swell region can be a significant proportion of $\Phi(\omega)$. However, its influence on the total dissipation is comparably less because the contribution of the wave frequency components is weighted by ω^2 [see Eqs. (4.11) and (4.12)], which favors the higher frequencies.

It is also important to point out that KHH assumed a single peak spectrum in developing the wave evolution equations. Their approach did not factor in the influence of swell on the dissipation. Since their model assumes that dissipation in deep water is due to wave breaking and since swell generally does not break (although swell may induce breaking of wind waves), extending the KHH-based formulas to include dissipation in the swell frequency range may overestimate the total dissipation. Nonetheless, the two time series in Fig. 16a show that the difference in the dissipation estimate using either approach is small.

2) D_P AND E_P

Clearly, the differences in the D_P and E_P estimates are more substantial than those between D_H and E_H. This is because E_P uses an equilibrium spectrum [Eq. (4.4)] assumption to model the measured wave spectrum, while the E_H model spectrum $\Phi_M(\omega)$ [Eq. (4.16)] is computed from the integral characteristics of the measured spectrum itself. The coefficients of Φ_M were chosen such that the measured and the idealized spectra have the same energy. Hence, the validity of our wave spectrum assumptions in computing E_H from the integral wind wave spectrum is based only on whether or not the slope of the wind wave portion of the measured spectrum Φ is close to ω^{-4}. Figures 9a and 16a show that this is a reasonable assumption. On the other hand, using Φ_E [Eq. (4.4)] in deriving E_P is based primarily on the validity of two assumptions: that the spectral slope of the equilibrium spectrum is indeed ω^{-4} and that the coefficient of ω^{-4} in Φ is $\alpha u_* g$. Equation (4.4) was obtained with the assumption that wind forcing, dissipation, and nonlinear spectral flux are in equilibrium balance under all wind and wave conditions.

In Fig. 9, we showed a normalized plot comparing 12 measured spectra and the equilibrium spectrum Φ_E [Eq. (4.4)]. In that figure, we saw that the magnitude and slope of the measured wave spectrum $\Phi(\omega)$ are comparable to those of $\Phi_E(\omega)$ between the wind wave peak ω_P and approximately $2.5\omega_P$. We can further examine the adequacy of $\Phi_E(\omega)$ in approximating the measured wave spectrum by comparing it to the idealized spectrum [Eq. (4.16)]

$$\Phi_M(\omega) = 3a_w^2\omega_p^3\omega^{-4} = 0.89a_w^2\bar{\omega}_w^3\omega^{-4}, \quad (4.19)$$

whose mean frequency and total energy are equal to those of the measured wave spectrum.

The variables in the coefficient of Φ_M are the sea surface variance a_w^2 and the mean wave frequency $\bar{\omega}_w$, while in the coefficient of ω^{-4} in Φ_E, u_* is a variable while both α and g are constants. We can examine how effective Φ_E is in modeling the measured wave spectrum by comparing the coefficients of Φ_E and Φ_M. Figure 17 shows a plot of $0.89a_w^2\bar{\omega}_w^3$ versus $\alpha u_* g$ using the data from the NOBS observation period with the data showing

$$\alpha u_* g = 0.89a_w^2\bar{\omega}_w^3 \pm \epsilon, \quad (4.20)$$

where $\alpha = 0.11$ and the error $\epsilon \approx 0.1$. The nature of the error is seen in Fig. 18a, which shows a plot of the time series of $0.89a_w^2\bar{\omega}_w^3$ and $\alpha u_* g$. Although the plot shows good agreement between the two parameters, clearly there are differences between the two. This

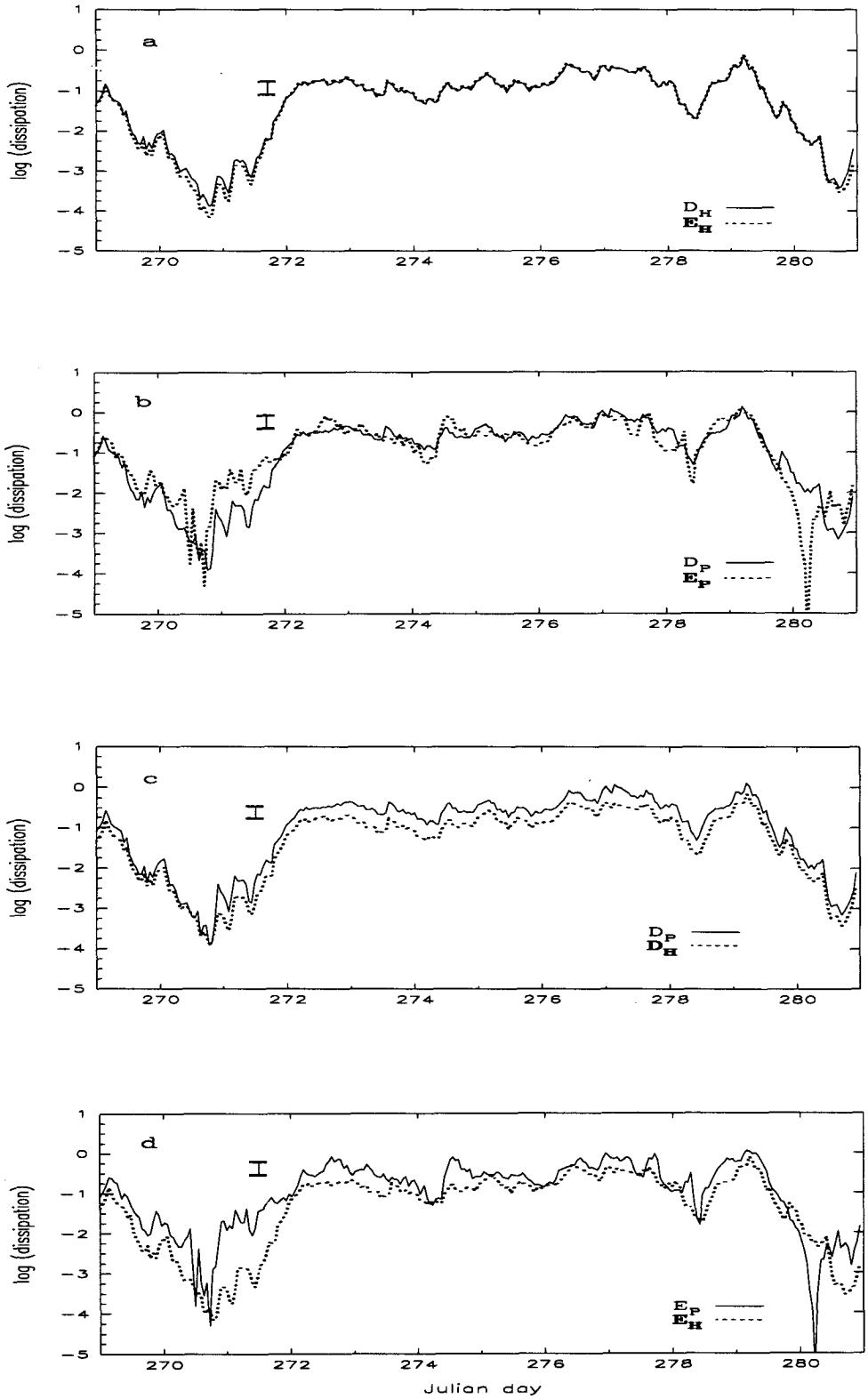

FIG. 16. Comparison of the time series of the log of the total dissipation [kg s^{-3}] computed using the formulas given in Table 7. Error bars denote the magnitude of the uncertainty in the empirical constants: (a) D_H (solid line) and E_H (short dash). (b) D_P (solid line) and E_P (short dash), (c) D_P (solid line) and D_H (short dash), (d) E_P (solid line) and E_H (short dash).

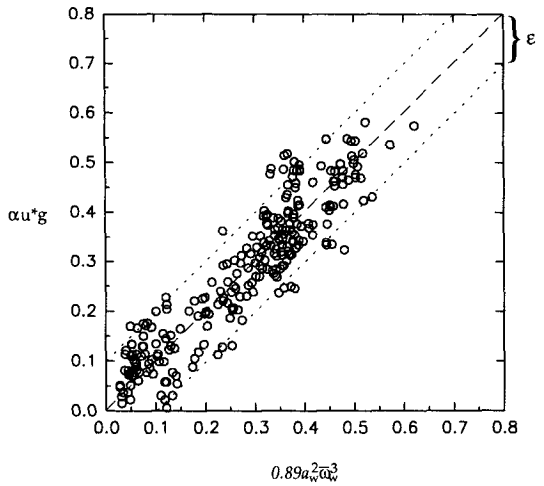

FIG. 17. Plot showing a good correlation between $0.89a_w^2\bar{\omega}_w^3$ and $\alpha u_* g$ [$m^2 s^{-3}$]. The regression line has a slope = 1 with $C_{xy} = 0.92$.

is demonstrated in Fig. 18b, which plots the difference between $0.89a_w^2\bar{\omega}_w^3$ and $\alpha u_* g$ normalized by $0.89a_w^2\bar{\omega}_w^3$. From this plot, we see that the discrepancy between $0.89a_w^2\bar{\omega}_w^3$ and $\alpha u_* g$ is large when their absolute values are small. Hence, the differences between $\alpha u_* g$ and $0.89a_w^2\bar{\omega}_w^3$ are significant during the early stages of wind and wave growth (Julian day 271). When the wind is decaying (Julian day 279–280), $\alpha u_* g$ can also significantly underestimate $0.89a_w^2\bar{\omega}_w^3$. The time series also shows that even under fully developed conditions, the wave field $0.89a_w^2\bar{\omega}_w^3$ may not respond quickly to rapid fluctuations in the wind speed $\alpha u_* g$.

The plots in Fig. 18 suggest that under fully developed and slowly varying wind and wave conditions, the Phillips (1985) equilibrium spectrum Φ_E adequately describes the wave field. Under conditions of rapid wind change, the assumption of local spatial and temporal equilibrium may not hold and the proportionality of the source terms [Eq. (4.2)] may not be strictly valid.

c. *Ambient noise correlation coefficients and power laws*

We now consider correlations between the ambient noise and our estimates of the surface wave dissipation. Figure 19 shows plots of the four dissipation estimates versus the ambient noise at 4.3 kHz. The plots show a good correlation between ambient noise N and the dissipation. The relationship between dissipation and N at the other frequencies show similar characteristics except for N(14 kHz) where noise contamination from the other instruments is more difficult to remove (see Fig. 2). For this reason, we will confine our discussion in this section to the other three noise frequencies given in the figures.

We also see that the dissipation data where $\log D > -1.5$ show considerably less scatter than data where $\log D < -1.5$. This is partly due to the distribution of the available data. In Fig. 10, we saw that the wind and wave conditions were quasi-steady with the wind speed and dissipation constant for approximately half of the observation period. As a result, the low N data are sparse and the data distribution is biased toward the higher wind speeds and dissipation values.

Except for E_P, the dissipation estimates were all computed directly from wave field parameters. Here E_H was computed from the variance of the wind wave field a_w^2 and the mean frequency $\bar{\omega}_w$, while D_H and D_P were computed from the measured spectra. Table 8 compiles the different regression equations for the various dissipation versus ambient noise plots. For purposes of this work, we adopted the form of the WOTAN equation to relate the dissipation D to ambient noise

$$\log D = m(f)N(f) + n(f). \qquad (4.21)$$

The coefficients m and n in Table 8 were computed using the orthogonal linear regression formula (Casella 1990, p. 586).

Equation (4.21) is equivalent to a power-law expression between the sound pressure and surface wave dissipation. We can therefore express it in terms of the equation

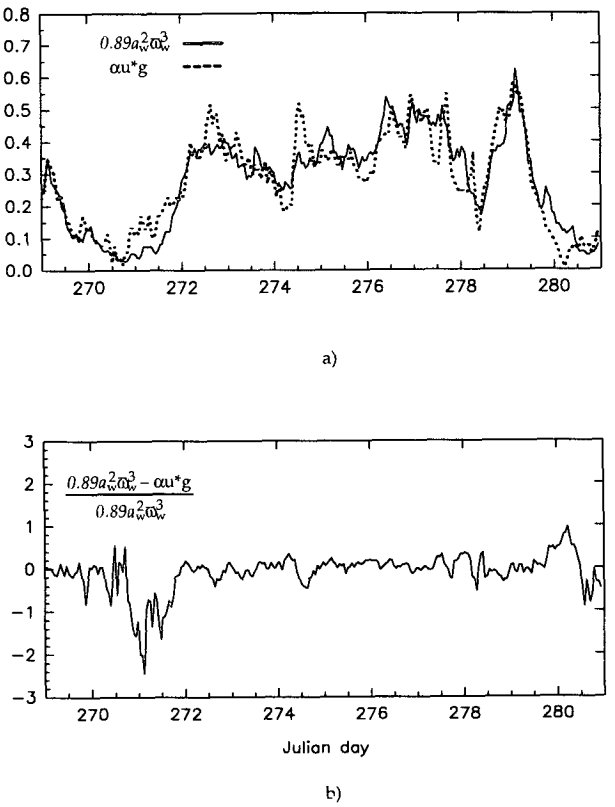

FIG. 18. (a) Plot showing the time series of the Φ_M and Φ_E coefficients: $0.89a_w^2\bar{\omega}_w^3$ (solid line) and $\alpha u_* g$ (short dash) [$m^2 s^{-3}$]. (b) Plot showing the relative magnitude of the difference between $0.89a_w^2\bar{\omega}_w^3$ and $\alpha u_* g$.

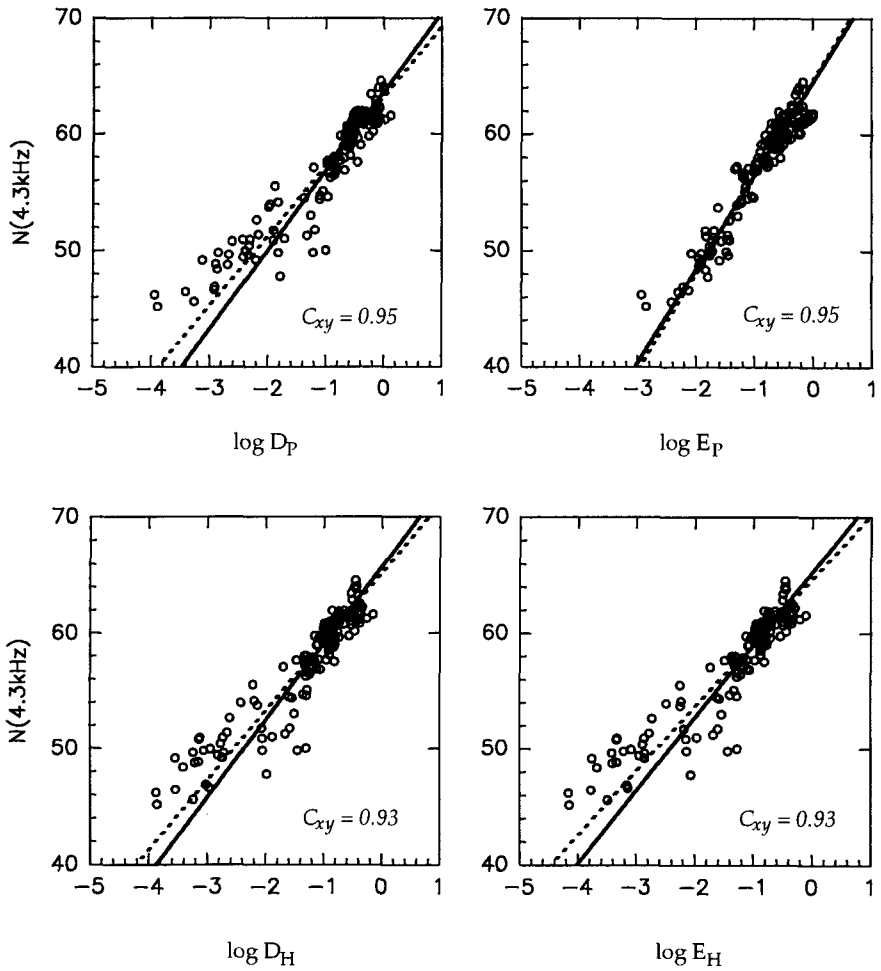

FIG. 19. Plots of the dissipation estimates computed using the equations in Table 7 [kg s^{-3}] vs N(4.3 kHz) (dB re 1 μPa^2/1 Hz). Regression equations over the entire range are denoted by dashed lines. Solid lines denote regression over data where wave breaking is visible ($N > 52$ dB). Also given are the correlation coefficients for the data in each plot C_{xy}, and the exponent n for the power law $p^2 \propto D^n$ given by each line.

$$\frac{p^2}{p_{\text{ref}}^2} = mD^n, \tag{4.21'}$$

where $m = 10^{-n/10m}$ and $n = 1/(10\text{ m})$. Our computations suggest that the power-law dependence between the ambient noise pressure level and dissipation over the entire range of the data is

$$p^2 \propto D^{0.5\text{–}0.6} \tag{4.22}$$

for the estimates computed from wave field characteristics (D_H, E_H, and D_P), and a slightly steeper power-law dependence

$$p^2 \propto D^{0.8}, \tag{4.23}$$

when the dissipation is computed from u_* and the wave age (E_P). The results show that dissipation correlates well with ambient noise in the field.

Video observations of the sea surface during the experiment showed that the onset of wave breaking is at $U_{10} \approx 5$ m s^{-1}. This corresponds to N(4.3 kHz) $\approx$ 52 dB re 1μPa^2/1Hz or log$D \approx -2$ where the unit of D is kg s^{-3}. Below that value, the equations in Table 7 give a nonzero dissipation estimate despite the absence of observable wave breaking. Hence, there is some uncertainty in the dissipation estimates below log$D \approx -2$. This is shown by the apparently larger scatter in the data at that range (Fig. 19).

If we limit the comparisons between the dissipation estimates with N(4.3 kHz) to the range where wave breaking is observable, the regression of the dissipation estimates computed from wave parameters (D_H, E_H, and D_P) give a slightly steeper slope with

$$p^2 \propto D^{0.6\text{–}0.7}. \tag{4.24}$$

TABLE 8. Coefficients for the ambient noise and dissipation expression, and the equivalent power laws computed from NOBS data for $\log D = m(f)N(f) + n(f)$ and $p^2/p_{ref}^2 = mD^n$.

f (kHz)	C_{xy}	m	n	$10^{-6}m$	n
		1) D_H			
4.3	0.93	0.167	−10.90	3.36	0.60
8.0	0.93	0.184	−10.99	0.94	0.54
14.0	0.81	0.207	−11.10	0.23	0.48
Σ	0.92	0.185	−15.52	245	0.54
		2) E_H			
4.3	0.93	0.181	−11.71	2.95	0.55
8.0	0.93	0.199	−11.80	0.85	0.50
14.0	0.81	0.223	−11.89	0.21	0.45
Σ	0.91	0.200	−16.71	226	0.50
		3) D_P			
4.3	0.95	0.166	−10.49	2.09	0.60
8.0	0.94	0.182	−10.55	0.63	0.55
14.0	0.79	0.201	−10.47	0.16	0.50
Σ	0.93	0.183	−15.04	165	0.55
		4) E_P			
4.3	0.95	0.121	−7.78	2.69	0.83
8.0	0.93	0.133	−7.83	0.77	0.75
14.0	0.79	0.152	−8.03	0.19	0.66
Σ	0.94	0.136	−11.28	197	0.74

For the Phillips (1985) equilibrium estimate E_P, the value of the exponent $n \approx 0.8$ is relatively unchanged.

5. Discussion

Several decades of research have demonstrated that the ambient noise N correlates well with wind speed in the Knudsen range. In contrast, research relating the ambient noise level to parameters of the wave field have been few and largely unsuccessful. Previous measurements have shown that N and the significant wave height (or the rms wave amplitude a) are poorly correlated.

The NOBS data show that while the rms surface wave amplitude a and N do not correlate well, we can improve the correlation between the two if we filter out the swell components from the sea surface elevation time series. When this is done, the correlation between N and the rms wind wave amplitude a_w is improved significantly (Fig. 13). This result suggests that the effect of swell on the sea surface variance a^2 is disproportionate to its effect on the frequency of wave breaking and consequently to N.

The measurements also show that a good linear correlation can also be found with ambient noise and the log of the spectral level of the wind wave frequencies (Fig. 14). Unlike a_w, the higher frequency wave components do not exhibit increased scatter in the data at low N and U_{10} values. They also give correlation coefficients with N that are slightly larger than those between N and a_w. Wind wave models (e.g., Phillips 1985) suggest that it is the waves at frequencies above the spectral peak that are responsible for most of the dissipation (see also Thorpe 1993; and Melville 1994). Clearly, the key to understanding the relationship between the ambient noise levels and the wave spectrum is in the higher wind wave frequencies.

The data show good correlations between the rms wave slope s and N as well (Fig. 15). This result appears to be consistent with experiments on laboratory-generated breaking waves (Rapp and Melville 1990; Melville et al. 1988; Loewen and Melville 1991), which show that the characteristic steepness of the wave field is the control parameter for many of the processes associated with wave breaking, including the sound radiated by the event.

In the absence of direct measurements of surface wave dissipation, we have used estimates based on Hasselmann's (1974) model, which is commonly used in the development of numerical wave evolution models, and Phillips's (1985) model, which is based on the assumption of equilibrium balance among the source terms. These models were discussed in some detail in section 4a. We found that while there are clearly differences between the two, they both give estimates that are comparable to one another over the range of conditions we encountered.

Both the KHH and the Phillips (1985) dissipation estimates can be computed from measurements of the surface wave spectrum. Their equations can be simplified by making assumptions about the characteristics of the wave spectrum and its relationship to wind and integral wave variables. With the Phillips (1985) model, this follows from the equilibrium balance assumption, which leads to

$$E_P \propto u_*^3 \ln[r(c_p/u_*)^2]. \tag{5.1}$$

The dependence on u_* is cubic while the influence of the wave field through the natural log of the wave age parameter is substantially weaker.

While KHH makes no assumptions on the form of the wave spectrum, we nevertheless simplified it by using the integral characteristics of the wave field to model the surface wave spectrum. Consequently, the nonconstant variables in the KHH estimate are the Pierson–Moskowitz steepness parameter $\bar{\alpha} = a_w^2 \bar{\omega}_w^4 / g^2$, the rms wind wave amplitude a_w, and the mean frequency $\bar{\omega}_w$. Rearranging Eq. (4.18) and evaluating $\bar{\alpha}$ gives

$$E_H \propto a_w^6 \bar{\omega}_w^9, \tag{5.2}$$

thus indicating that, using the KHH model, the total dissipation of the wave field can be computed from integral wind wave field characteristics.

It should be emphasized that the Phillips (1985) and the KHH equations are estimates rather than

measurements of dissipation. A key assumption in both these models is that the dissipation from wave breaking is a function of the surface wave spectrum Φ. The main weakness of this assumption is that at low wind speeds where there is no breaking, the value of Φ is nonetheless finite and nonzero. Hence, these models give a nonzero estimate of dissipation from wave breaking even in the absence of breaking waves.

The measurements reported here show that the mean square acoustic pressure p^2, which is proportional to the radiated acoustic power, is proportional to D^n where $n = 0.5$–0.8. The estimates based on surface wave parameters give values of n closer to the lower limit of that range. Low wind speed data for this experiment, however, is relatively sparse. If we consider only the higher wind speed data where wave breaking is observed, the data regressions give $n = 0.6$–0.8. In contrast, our laboratory experiments have shown that the radiated power is approximately proportional to D (Melville et al. 1988; Loewen and Melville 1991). Given the uncertainty in the model estimates of D, the possible propagation losses through the surface bubble layer, and the relatively small number of low wind speed data, the apparent differences between the laboratory and field measurements deserve further investigation.

In this regard, it is important to note that the majority of this dataset corresponds to quasi-steady sea state and wind conditions, which do not provide sufficient variability to conclusively determine the relationship between D and the ambient noise level N. The variability in D and N, which permits an empirical estimation of the relationship, comes from two relatively short periods of changing wind and wave conditions. Thus, more extensive measurements in a variety of environmental conditions will be required to firmly establish the relationship between D and N in the field.

One of the key issues in understanding the processes associated with air–sea interaction is how the wave field affects the air–sea boundary conditions and fluxes. One of the major obstacles in achieving this is our ability to quantify and characterize the wave breaking process. Our results suggest that the relationship between ambient noise and wave breaking may prove to be an important tool in quantifying surface wave dissipation in the field.

Acknowledgments. We thank John Hildebrand (SIO), the NOBS scientific party, and the crew of RP *FLIP* for making these measurements possible. The environmental data were supplied by Jerome Smith and Greg Bullard (SIO). Anatol Rozenberg provided helpful advice on the design of the directional hydrophone. This research was supported by a grant from the Office of Naval Research (Acoustics).

APPENDIX

The Effect of *FLIP* Motion on the Wave Gauge Record

The wire wave gauge measurements during NOBS were contaminated by the heave and pitch–roll motion of *FLIP*. The influence of *FLIP* on our wave measurements is primarily due to the motion of the point on the boom at which the wave gauge is attached. Here we examine the magnitude of the required correction to account for the motion of the boom.

As seen in Fig. 5, much of the energy associated with the motion of *FLIP* is manifested by the spectral peak corresponding to the heave (27-s period) and pitch–roll (48-s period) resonance of *FLIP*. The typical swell period is of the order 10 s. Most of the swell we observed during NOBS is of this magnitude. By choosing to neglect waves with period significantly longer than swell, it is relatively simple to correct for *FLIP* motion in this region by high-pass filtering the signal at $\omega = 0.1\pi$ rad s^{-1}.

Correcting for the energy at higher frequencies using accelerometer data poses a greater challenge. The apparent acceleration measured by a horizontal accelerometer is equal to the true acceleration plus the gravitational component in that direction. At very low frequencies, the value of the apparent acceleration is almost exclusively due to tilt. Rudnick (1967) suggested that at higher frequencies, four-fifths of the apparent acceleration can be attributed to true acceleration and one-fifth to tilt. However, he showed no actual measurements to support this.

For illustration purposes, we assume that the apparent acceleration measured by the accelerometers is due exclusively to tilt. This approach is conservative because it overestimates the required correction. The procedure is then relatively straightforward. From the accelerometer record, the tilt angles in the x and y axes are

$$\sin\theta_i \approx \theta_i = (\ddot{x}_i/g), \tag{A1}$$

where $\ddot{x}_i$ is the measured apparent acceleration in direction i and θ is in radians. For a point on *FLIP* at a location $(x, y, z) = (L_x, L_y, H)$ measured from the center of gravity, the vertical displacement of the point is given by

$$\delta_z = L_x \sin\theta_x + L_y \sin\theta_y - H(1 - \cos\theta_x) - H(1 - \cos\theta_y). \tag{A2}$$

In evaluating Eq. (A.2), we used $(L_x, L_y, H) = (7.7, 15.1, 42.7)$ m. The true sea surface elevation that should be measured by a wire wave gauge suspended at that point is therefore

$$a_{\text{true}}(t) = a(t) - \delta_z(t), \tag{A3}$$

where $a(t)$ is the sea surface elevation measured by the wire. Most of the spectral energy of δ_z is in the

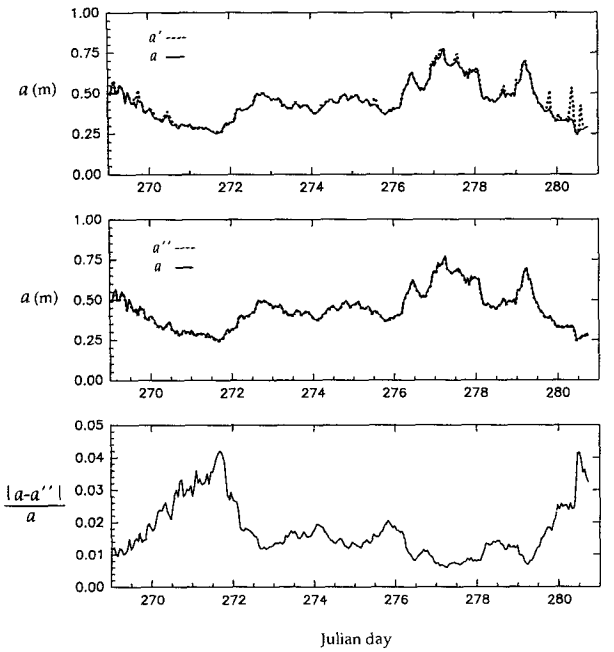

FIG. A1. Plots showing the influence of *FLIP* motion on the rms wave amplitude a of the wave gauge record. (a) Time series comparing the rms amplitude of the raw data a' (dashed line) and with the data high passed at $\omega/2\pi = 0.05$ Hz a (solid line). (b) Time series comparing the rms amplitude of a (solid line) with that of the "corrected" data a'' (dashed line). The two time series are practically indistinguishable. (c) The error associated with this correction is less than 5% of a.

resonant frequency peaks below $\omega = 0.1\pi$ rad s^{-1}. High-pass filtering at this frequency removes most of the energy due to δ_z. Figure A1a shows the time series of the raw rms wave amplitude a' and the rms wave amplitude of the high-pass filtered data a. We see from this figure that while the unfiltered and filtered estimates are close most of the time, there are portions of the time series where the value of a' significantly exceeds a.

Figure A1b examines the influence of the Eq. (A.3) "correction" on the rms wave amplitude. In this figure, the "corrected" data is denoted by a''. Before computing both a and a'', the data was high passed at 0.05 Hz. The two values are very close to each other and track each other well. Since the two time series are difficult to distinguish, we instead plot the difference between the a and a'' and normalize this by a. This is shown in Fig. A1c. In this figure, we see that the a'' differs from a by less than 5% for low wind speeds and by approximately 1% under fully developed conditions.

Note added in proof. Since this paper was accepted for publication, in closely related work, Ding and Farmer (1994a,b) have used ambient sound to track and quantify breaking waves and have attempted to relate the acoustic source level to dissipation by breaking.

REFERENCES

Bronson, E. D., and L. R. Glosten, 1985: FLIP: Floating Instrument Platform. SIO Reference 85-21. Revision of previous SIO Reference 73-30 by C. B. Bishop and D. O. Efird.

Casella, G., 1990: *Statistical Inference.* Wadsworth and Brooks, 650 pp.

Ding, L., and D. M. Farmer, 1994a: Observations of breaking surface wave statistics. *J. Phys. Oceanogr.*, **24,** 1368–1387.

——, and ——, 1994b: On the dipole acoustic source level of breaking waves. *J. Acous. Soc. Amer.*, **96,** 3036–3044.

Evans, D. L., D. R. Watts, D. Halpern, and S. Bourassa, 1984: Ocean winds measured from the seafloor. *J. Geophys. Res.*, **89,** 3457–3461.

Farmer, D. M., and D. D. Lemon, 1984: The influence of bubbles on ambient noise in the ocean at high wind speeds. *J. Phys. Oceanogr.*, **14,** 1762–1778.

——, and S. Vagle, 1988: On the determination of breaking surface wave distributions using ambient sound. *J. Geophys. Res.*, **93,** 3457–3461.

——, and ——, 1989: Wave propagation of ambient sound in the ocean-surface bubble layer. *J. Acoust. Soc. Amer.*, **86,** 1897–1908.

Felizardo, F. C., 1993: *Ambient Noise and Surface Wave Dissipation in the Ocean.* Ph.D. thesis, Massachusetts Institute of Technology/Woods Hole Oceanographic Institution, Cambridge, MA.

Hasselmann, K., 1962: On the nonlinear transfer of energy in the peak of a gravity wave spectrum. Part 1. *J. Fluid Mech.*, **12,** 481–500.

——, 1963: On the nonlinear transfer of energy in the peak of a gravity wave spectrum. Parts 2 and 3. *J. Fluid Mech.*, **15,** 273–281, 385–398.

——, 1974: On the spectral dissipation of ocean waves due to white-capping. *Bound.-Layer Meteor.*, **6,** 107–127.

Kennedy, R. M., 1992: Sea surface dipole sound source dependence on wave-breaking variables. *J. Acoust. Soc. Amer.*, **91,** 1974–1982.

Kerman, B. R., 1988: *Sea Surface Sound: Natural Mechanisms of Surface Generated Noise in the Ocean.* Kluwer Academic, 639 pp.

——, 1992: *Natural Physical Sources of Underwater Sound: Sea Surface Sound (2).* Kluwer Academic, 749 pp.

Keulegan, J. H., 1951: Wind tides in small closed channels. *J. Res. Natl. Bur. Stand.*, **46,** 358–381.

Knudsen, V. O., R. S. Alford, and J. W. Emling, 1948: Underwater ambient noise. *J. Mar. Res.*, **7,** 410–429.

Komen, G. J., S. Hasselmann, and K. Hasselmann, 1984: On the existence of a fully developed wind-sea spectrum. *J. Phys. Oceanogr.*, **14,** 1271–1285.

Lamarre, E., and W. K. Melville, 1991: Air entrainment and dissipation in breaking waves. *Nature,* **351,** 469–472.

Lemon, D. D., D. M. Farmer, and D. R. Watts, 1984: Acoustic measurements of wind speed and precipitation over a continental shelf. *J. Geophys. Res.*, **89,** 3462–3472.

Loewen, M. R., and W. K. Melville, 1991: Microwave backscatter and acoustic radiation from breaking waves. *J. Fluid Mech.*, **224,** 601–623.

Longuet-Higgins, M. S., 1952: On the statistical distribution of the heights of sea waves. *J. Mar. Res.*, **11,** 245–266.

Maat, N., C. Kraan, and W. A. Oost, 1991: The roughness of wind waves. *Bound.-Layer Meteor.*, **54,** 89–103.

Melville, W. K., 1994: Energy dissipation by breaking waves. *J. Phys. Oceanogr.*, **24,** 2041–2049.

——, M. R. Loewen, F. C. Felizardo, A. T. Jessup, and M. J. Buckingham, 1988: Acoustic and microwave signatures of breaking waves. *Nature,* **336,** 54–59.

Miles, J. W., 1957: On the generation of surface waves by shear flows. *J. Fluid Mech.*, **3,** 185–204.

Penhallow, W. S., and F. T. Dietz, 1964: Correlation of 630-cps shallow-water ambient noise with wind speed and waveheight. *J. Acoust. Soc. Amer.*, **36,** 2149–2151.

Perrone, A. J., 1969: Deep-ocean ambient noise spectra in the northwest Atlantic. *J. Acoust. Soc. Amer.*, **46,** 762–770.

Phillips, O. M., 1985: Spectral and statistical properties of the equilibrium range in wind-generated gravity waves. *J. Fluid Mech.*, **156,** 505–531.

Plant, W. J., 1982: A relationship between wind stress and wave slope. *J. Geophys. Res.*, **87,** 1961–1967.

Rapp, R. J., and W. K. Melville, 1990: Laboratory measurements of deep-water breaking waves. *Philos. Trans. Roy. Soc. London A,* **331,** 735–800.

Rudnick, P., 1967: Motion of a large spar buoy in sea waves. *J. Ship Res.*, 257–267.

Shaw, P. T., D. R. Watts, and H. T. Rossby, 1978: On the estimation of oceanic wind speed and stress from ambient noise measurements. *Deep-Sea Res.*, **25,** 1225–1233.

Snyder, R. L., F. W. Dobson, J. A. Elliot, and R. B. Long, 1981: Array measurements of atmospheric pressure fluctuations above surface gravity waves. *J. Fluid Mech.*, **102,** 1–59.

Thorpe, S. A., 1993: Energy loss by breaking waves. *J. Phys. Oceanogr.*, **23,** 2498–2502.

Urick, R. J., 1986: *Ambient Noise in the Sea.* Peninsula Publishing, 160 pp.

Vagle, S., W. G. Large, and D. M. Farmer, 1990: An evaluation of the WOTAN technique of inferring oceanic winds from underwater ambient sound. *J. Atmos. Oceanic Technol.*, **7,** 576–595.

WAMDIG, 1988: The WAM model—a third generation ocean wave prediction model. *J. Phys. Oceanogr.*, **18,** 1775–1810.

Wenz, G. M., 1962: Acoustic ambient noise in the ocean: Spectra and sources. *J. Acoust. Soc. Amer.*, **34,** 1936–1956.